Journal of the Energy Institute 119 (2025) 101977

Contents lists available at ScienceDirect

Journal of the Energy Institute

journal homepage: www.elsevier.com/locate/joei

Carbon conversion mechanism of volatile gas flame based on multi-spectral analysis methods

Xiao Lin [a,b], Meirong Dong [a,b,*], Gangfu Rao [c], Wei Nie [d], Guangchi Zhou [a,b], Jidong Lu [a,b]

[a] School of Electric Power, South China University of Technology, Guangzhou, Guangdong, 510640, China
[b] Guangdong Province Engineering Research Center of High Efficient and Low Pollution Energy Conversion, Guangzhou, Guangdong, 510640, China
[c] School of Mechanical and Electronic Engineering, Jingdezhen University, Jingdezhen, Jiangxi, 333032, China
[d] AnHui Institute of Optics and Fine Mechanics, HeFei Institutes of Physical Sciences, Chinese Academy of Sciences, Hefei, 230031, China

ARTICLE INFO

Handling Editor: Dr. Paul Williams

Keywords:
Volatile flame
Carbon conversion
Multispectral analysis
Chemical kinetic analysis

ABSTRACT

Volatile combustion is a critical process in solid fuel combustion, requiring a deeper understanding of its carbon conversion mechanisms. This study investigates the synergistic effects of different volatile fraction components CH_4, CO, C_2H_4, and H_2 on carbon conversion using a McKenna flat-flame burner. The spatial distribution characteristics of excited-state radicals in flames, namely OH*, CH*, and C_2*, were qualitatively measured using image spectroscopy. Additionally, the final product H_2O concentration and flame temperature were quantitatively determined through Tunable Diode Laser Absorption Spectroscopy (TDLAS). Combined with chemical kinetics simulations, the study reveals the volatile combustion reaction pathways and the synergistic effects of multi-component co-combustion on carbon conversion. The experimental and kinetic analysis results indicate that H_2 promotes CH_2 and CH formation, thereby facilitating the production of C_2* and OH*. C_2H_4 enhances C_2H formation, which promotes the production of CH*. Additionally, H_2 increases H_2O production and raises temperature in flame, while CO inhibits both. While maintaining consistent combustible carbon content in fuel, H_2 primarily inhibits the carbon conversion from fuel to CO_2 by reducing the pathway proportions involving the main chain reactions HCO and CO, as well as the branch reactions CH_2* and CH_2. In contrast, CO and C_2H_4 promote carbon conversion to CO_2 by increasing the pathway proportions of the branch reactions CH_2* and CH_2. When multi-component co-combustion, the gain in pathway proportion is influenced by both individual component effects and complex synergistic effects, which may result in various outcomes such as synergistic promotion, synergistic inhibition, or a simple additive effect.

1. Introduction

Solid fuels, such as coal and biomass, are a major component of primary energy composition. The combustion of solid fuels involves complex gas-solid phase reaction processes, including devolatilization, volatile combustion and char combustion [1–3]. The combustion of volatile gases, involving various physical changes and chemical reactions, is a critical stage in the overall fuel combustion process. The volatile gases of fuels like biomass primarily include CH_4, CO, H_2, and C_2H_4, etc [4–6]. One of the main products of volatile combustion is CO_2, which has been identified as a significant contributor to the greenhouse effect. The increase in atmospheric CO_2 concentration has been linked to global warming and climate change. Therefore, it is essential to conduct the comprehensive study of the carbon conversion mechanisms during the combustion of volatile gases in order to optimize the combustion process, improve combustion efficiency, and reduce CO_2 emissions.

The most commonly used traditional thermal analysis methods for studying solid fuel volatile combustion are thermogravimetric analysis (TGA) and tube furnace heating analysis. TGA measures the mass loss of a sample as temperature increases, providing insights into the patterns of fuel devolatilization and combustion. Ye et al. [7] utilized TGA to investigate the co-combustion characteristics of coal and microalgae under different blending ratios and atmospheres, revealing that the height of the volatile matter flame is influenced by both the release rate and the combustion rate of volatile matter. On the other hand, tube furnace experiments offer conditions that more closely resemble actual

* Corresponding author. School of Electric Power / Guangdong Province Engineering Research Center of High Efficient and Low Pollution Energy Conversion, South China University of Technology, Guangzhou, Guangdong, 510640, China.
E-mail address: epdongmr@scut.edu.cn (M. Dong).

https://doi.org/10.1016/j.joei.2025.101977
Received 18 October 2024; Received in revised form 25 December 2024; Accepted 2 January 2025
Available online 4 January 2025

combustion environments. By precisely controlling temperature and atmosphere, the tube furnace experiments simulate the high-temperature combustion of volatile. Khatami et al. [8] used an electrically heated drop tube furnace to examine the combustion of coal powders of different grades, observing that volatile combustion temperature is affected by both coal grade and temperature conditions. Liang et al. [9] used a transparent visual drop-tube furnace to investigate the combustion behavior of single particles of eucalyptus, pine and olive residues and found that the ratio of coke burnout time to volatile combustion time correlated well with the fixed carbon to volatile mass ratio.

Traditional thermal analysis methods typically analyze volatile combustion based on the overall mass loss or product formation of fuels, making it difficult to capture the dynamic changes of flame characteristics and intermediates. In contrast, non-contact optical measurement methods enable in situ measurement of components and characteristic parameters within the flame. Optical measurement techniques have become a key tool for in situ monitoring of combustion flow fields and have played an important role in combustion diagnostics and mechanistic studies. Due to the differing principles of various optical detection technologies, their focus on detection targets also varies. Common optical diagnostic techniques include imaging spectroscopy and laser spectroscopy.

Imaging spectroscopy is a passive measurement method that utilizes optical devices such as CCDs to collect flame signals. On one hand, it can measure flame characteristics, including flame morphology, flame speed, and radiative properties. Lee et al. [10] used a high-speed camera to capture real-time images of volatile matter flames from sub-millimeter fuel particles and analyzed the effects of fuel type and atmospheric conditions on fuel ignition and flame morphology. Zhu et al. [11] investigated the devolatilization combustion of coal particles on a McKenna flat-flame burner, using a visible-light camera to observe the time-resolved evolution of volatile flames. Selle et al. [12] measured laminar flame velocity of methane/air flames using a two-dimensional slot burner and discussed the limitations of this method to measure the flame velocity for other mixtures. Zheng et al. [13] measured the temperature and emissivity distributions of volatile flames from different types of biomass using flame emission spectroscopy and found that the radiative properties of these flames do not change with biomass species and combustion conditions. On the other hand, imaging spectroscopy can also obtain intermediate species information through the analysis of the chemiluminescence signals of flames [14,15]. Kojima et al. [16] used a resolution-enhanced Cassegrain-type optical probe to measure the OH*, CH*, and C_2* emission patterns in a CH_4/air laminar premixed flame and established a correlation between the OH*/CH* chemiluminescence peak intensity ratios and the flame equivalence ratio. Wang et al. [17] used a lens-based fiber coupled with a spectrometer to quantitatively measure the chemiluminescence of OH*, CH*, and C_2* in a CH_4/air premixed flame and found that the emission intensity of CH* and OH* were in the same order of magnitude.

While passive imaging spectroscopy is widely used for flame characteristic analysis due to its ease of operation and ability to effectively measure intermediate products, the reliance on chemiluminescence signals from the flame limits its spectral resolution and sensitivity. In contrast, laser spectroscopy, as an actively excited optical detection method, offers higher sensitivity and resolution, making it advantageous for precise measurements of species concentrations and temperatures. Among the laser spectroscopy techniques, tunable diode laser absorption spectroscopy (TDLAS) can quantitatively measure temperature and target component concentrations in combustion fields [18,19]. Sentko et al. [20] used diode lasers with center wavelengths of 1344 nm, 1392 nm, and 1853 nm to simultaneously measure the H_2O concentration and temperature in CH_4-rich oxygen flames. Liu et al. [21] used a diode laser with an emission wavelength of 1.4 μm to collect two H_2O absorption lines for temperature measurement, achieving a measurement error of less than 4 % in a McKenna flat-flame burner.

Planar laser-induced fluorescence (PLIF) is another laser spectroscopy technique commonly used for flame diagnostics. It enables high-resolution detection of the spatial distribution and dynamic evolution of key combustion radicals and small molecular products by exciting them with ultraviolet lasers of specific wavelengths (e.g., 266 nm, 283 nm, or 355 nm). Kumar et al. [22] utilized high-frequency OH-PLIF imaging to investigate the transient dynamics and three-dimensional characteristics of bluff-body flame extinction, capturing the evolution of OH radical distribution and the dynamic behavior of the flame front. Additionally, they developed a multi-laser beam intensity distribution correction method, further enhancing the measurement accuracy of PLIF under complex combustion conditions [23]. Chaib et al. [24] obtained high-resolution images of turbulent flame fronts using PLIF and developed a hybrid detection algorithm that significantly improved the reliability of flame front identification. Tanahashi et al. [25] combined CH-OH PLIF with stereoscopic particle image velocimetry (PIV) techniques to conduct synchronized measurements of the three-dimensional structure of turbulent premixed flames and their coupling with turbulent flow fields. Rao et al. [26] used image spectroscopy, TDLAS, and planar laser-induced fluorescence (PLIF) to obtain the spatial distribution characteristics of the major excited-radicals (C_2*/CH*/CN*/OH*), H_2O, and NO, respectively, in NH_3-doped methane flames, respectively.

To further reveal the reaction pathways, chemical kinetic analysis can be combined to identify the key fundamental reactions and gain insight into the generation and consumption of intermediate products, thereby revealing the carbon conversion mechanisms during the volatile combustion process. The volatile gases that are released during the devolatilization of solid fuels have complex compositions, and the carbon conversion process is influenced by various factors. In recent years, research on volatile flame has gradually shifted from directly using complex solid fuels to employing model compounds as substitutes for volatiles. By selecting typical components from volatile gases to form model compounds, researchers can explore the combustion characteristics, reaction pathways, and product distribution of volatile flames under more controlled conditions. Taniguchi et al. [27] simplified the combustion of the coal volatile fraction as a premixed combustion of methane and hydrogen gas and investigated the NOx generation pattern under different equivalence ratios. Xia et al. [28] simulated the combustion of volatile gases using a mechanism including an $H_2/CO/C_1$-C_4 mechanism and found that the fuel/air equivalence ratios were positively correlated with laminar flame velocity and flame temperature. Wang et al. [29] analyzed the CH_4/H_2/air combustion process using the AramcoMech mechanism. Through global pathway (GP) analysis and sensitivity analysis of the physical parameters of each species, they found that fuel oxidation is dominated by different GPs at varying hydrogen mole fraction, and each GP exhibits dominance in different flame temperature regions. Zhang et al. [30] conducted numerical simulations of oxygen-enriched methane/air flames with different equivalence ratios using the GRI 3.0 mechanism. They analyzed the NO formation characteristics and investigated the kinetic impact of oxygen enrichment on the flame reaction pathways. It was found that oxygen enrichment significantly affects the oxidation process of CH_3, notably enhancing the reactions associated with the consumption of O, OH, and H.

To reveal the synergistic effects of volatile fraction components on carbon conversion pathways, this study focuses on the typical volatile components $CH_4/CO/C_2H_4/H_2$/air premixed flat flames, utilizing in-situ multispectral measurement techniques and chemical kinetics simulations. The spatial distribution of major excited radicals OH*, CH*, and C_2* was qualitatively measured using imaging spectroscopy, while TDLAS was employed to quantitatively measure the concentration of the final product H_2O and the flame temperature. Based on a comprehensive understanding of combustion intermediates, final products, and the thermodynamic parameter temperature, the volatile flames are modeled using the optimized GRI 3.0 kinetic mechanism. The simulation enables detailed analysis of the reaction pathways, identification of key

elementary reactions, and the formation and consumption of intermediate products, thus revealing the effects of multi-component synergistic combustion on the carbon conversion pathways in the flames.

2. Methods and experimental

2.1. Experiment setup

The multispectral gas flame measurement system consisted of an optical measurement system and a combustion system, as shown in Fig. 1. The combustion system consisted of a McKenna burner (Holthuis & Associates) and a gas supply system. The McKenna burner used in the experiment has an outer diameter of 120 mm and an overall height of 63.5 mm [31,32]. The burner exit surface was constructed from sintered fine bronze beads, with a diameter of 60 mm and a 5.5 mm width shroud ring. A water-cooling system was incorporated to maintain the initial temperature at 300 K. Fuels and air were mixed in a mixer before being introduced into the McKenna burner via fuel nozzles. Pure nitrogen, acting as a protective gas, flowed out of the shroud ring at a rate of 10 L/min. The flow rates of gases were controlled by flow meters, and these gases were premixed in an air mixer to form a stable laminar premixed flat flame on the burner. The burner was mounted on a translation stage, allowing the position measured by the optical measurement system to be controlled by adjusting the electrical translation stage.

The gases used in this experiment have a purity of 99.999 %. Sevenstar CS200 flowmeters were employed, each with an accuracy of ±1.0 % of the set point (SP) for flow rates ≥35 % of full scale (FS), and ±0.35 % of FS for flow rates <35 % FS. Flow rate errors are directly related to the set point or full scale, and these errors were accounted for and corrected during the experimental calibration process to ensure accurate control of flow rate measurements. The influence of systematic errors on the experimental results was reduced by repeating the experiment several times.

The optical measurement system consisted of image spectroscopy detection device and the TDLAS system. The image spectroscopy is a qualitative planar measurement technique that utilized an ICCD camera (DH734, Andor, 1024 × 1024 pixels) coupled with narrowband filters, selecting appropriate gate widths, exposure times, and gains to detect the radiation spectra of the excited-state radicals OH*, CH*, and C_2* in the flame. The center wavelengths of the filters capturing OH*, CH*, and C_2* were 315 nm, 434 nm, and 514.5 nm, respectively. A bandpass filter (FGUV11, Thorlabs) was used to reduce the interference of the yellow-green light with the spontaneous radiation of OH*. For OH* imaging, the exposure time and gate width were both set to 1000 ms, with a gain of 500. For CH* imaging, the exposure time and gate width were both set to 2000 ms, with a gain of 500. For C_2* imaging, the exposure time and gate width were both set to 3000 ms, with a gain of 1000. The gain of the ICCD camera was carefully adjusted to optimize the signal-to-noise ratio while avoiding saturation. Background correction was performed by capturing images in the absence of a flame and subtracting these from the measured flame images to eliminate noise and stray light effects. The intensity averages of 20 spectra were used for the analysis to minimize the effect of random errors on the measurements.

TDLAS is a line-of-sight measurement technique based on the absorption spectra of target molecules. It uses laser beams of specific wavelengths to detect the average concentration and temperature distribution of gases along the optical path. By utilizing the absorption characteristics provided by the HITRAN database, TDLAS accurately retrieves the temperature distribution and derives the gas species concentrations. The TDLAS system mainly consisted of a function generator, laser controller, distributed feedback (DFB) diode lasers, detector, and data acquisition module for the quantitative measurement of the concentration of the final product H_2O in the combustion field and temperature detection by the two-line method. With a narrow linewidth and high tuning stability, DFB lasers facilitate high-resolution and highly selective gas absorption spectroscopy measurements. During the experiment, a sawtooth wave current generated by the function generator caused the DFB laser, with center wavelengths of 1343 nm (7444 cm^{-1}) and 1392 nm (7185 cm^{-1}), to emit continuous laser light. The laser light passing through the flame was received by the detector, which obtains the laser attenuation signal. The detector signal was collected by the data acquisition module after passing through the transmission module. The spatial resolution of the measurements is set to 1 mm to obtain detailed spatial distribution information. When the flame was stabilized, TDLAS system was utilized for 1-min measurements at each position. The TDLAS system based on DFB lasers has a sampling frequency of 1000 Hz. During steady-state flame measurements, the collected spectral data are averaged to ensure accuracy and reliability.

In this study, two independent optical techniques, imaging spectroscopy and TDLAS, were employed to investigate the steady-state flame on a McKenna burner. Due to the high stability and lack of temporal variation in the optical signals of the steady-state flame, reliable data could be obtained without the need for synchronized measurements. Imaging spectroscopy was used to capture the two-dimensional distribution of excited-state radicals in the flame [33], while TDLAS was applied to accurately measure the concentration distribution and temperature of specific components [34]. Since these two methods target different spectral ranges and signal characteristics, their optical paths and signal acquisition processes are entirely independent, ensuring no interference and guaranteeing the independence and

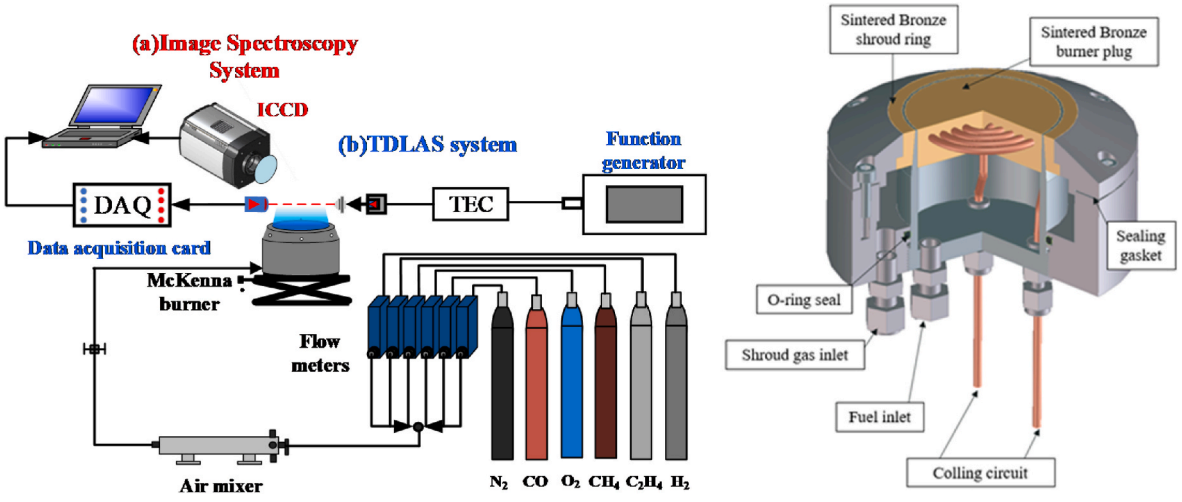

Fig. 1. Experimental setup diagram.

accuracy of the data. The uncertainty in experimental measurements primarily originates from flowmeter and TDLAS measurement errors. TDLAS measurements are highly sensitive to gas concentration, and the effects of temperature and pressure fluctuations on the shape and strength of the absorption lines have been taken into account in the choice of the Voigt function to ensure that the measurement error was within 0.5 %. The experiments were carried out under steady-state conditions with the flow rate controlled within ±1 %, which ensured the consistency of the proportions of the gas mixtures. In addition, the reliability and stability of the experimental data were ensured by multiple repetitions of the experiments and averaged spectral analysis.

2.2. Experimental condition

In this work, we used the typical components of volatile light gases as substitutes for the actual volatile fractions produced from fuel devolatilization. The syngas composition includes CH_4, C_2H_4, CO and H_2, which represent saturated hydrocarbons, unsaturated hydrocarbons, combustible carbon-oxygen compounds, and carbon-free high calorific value gases in volatile light gases, respectively. The ratio of each component was set according to the concentration range of the components in the volatile gases [35–37], where the concentration of CO was set at 4500 ppm, the concentration of H_2 was set at 3500 ppm, and the concentration of C_2H_4 was set at 1500 ppm. The flames were composed of the base flame part and the multi-component coexisting flame part. The base flame was consistent in all cases, and the flame equivalence ratio was set to 1. The components of the multi-component coexisting flame are listed in Table 1. CH_4 was added to the multi-component coexisting flame part to ensure the same combustible carbon content of the initial reactants. In the multi-component coexisting flame part, the fuel-equivalent air was adjusted to maintain the flame equivalence ratio of 1, while the total flow rate was maintained by adjusting the N_2 flow rate. Different combinations of coexisting gases were employed to simulate the multi-component coexisting combustion scenario during the combustion of volatiles in the biomass pyrolysis process.

2.3. Kinetic modeling

To investigate the changes in reaction pathways and rates under different cases of volatile components coexistence, the Premix Laminar Flame-Speed Calculation module of Chemkin-Pro was used to simulate the volatile flame on the McKenna burner, using the GRI-Mech 3.0 mechanism for chemical kinetics analysis. The pressure was set to atmospheric (1 atm) and the grid parameters CURV and GRAD were set to 0.02.

The GRI-Mech 3.0 mechanism, widely used for simulating natural gas flames, includes the chemical kinetics mechanisms of typical components such as CH_4, C_2H_4, CO, and H_2, and has been extensively validated in studies of syngas flames [38,39]. While the GRI-Mech 3.0 model provides a comprehensive description of the overall mechanism of methane oxidation, it does not fully account for the processes of excited-state free radical (OH*、C_2* and CH*) formation and quenching, which play a critical role in intermediate product formation, flame chemical activity, and spectral diagnostics during combustion.

OH*、C_2* and CH* are widely used in the diagnosis and mechanism studies of combustion processes due to their significant chemiluminescent characteristics in flame [40–42]. Among them, the chemiluminescence of OH* serves as a critical indicator of high-temperature oxidation reactions and is closely related to heat release processes and flame stability. Meanwhile, the chemiluminescence of C_2* and CH* reveals the decomposition mechanisms of intermediate species, providing key insights into the primary reaction pathways of volatile components. Specifically, the C_2* radical is regarded as an effective tracer for hydrocarbon combustion pathways, while the CH* radical, as a key intermediate at the flame front, is intricately linked to the decomposition behavior during the early stages of combustion.

To address this limitation, this study extends the GRI-Mech 3.0 model by incorporating elementary reactions related to the formation and quenching of excited-state free radicals to address the key limitation of the original model, guided by spectral experimental data, as shown in Table 2.

3. Results and discussion

3.1. Spatial distribution of excited-state radicals based on image spectroscopy

Radicals are key indicators of intermediate processes in the carbon conversion within volatile flames. The spontaneous emission of the main excited-state radicals (OH*, CH*, and C_2*) in the flame can be obtained by imaging spectroscopy, thereby enabling an analysis of the effects of different components coexistence conditions on the generation of excited-state radicals in volatile flames. The radical spectra of OH*, CH* and C_2* are shown in Fig. 2.

As shown in Fig. 2, the spectral intensity peaks of each radical are concentrated in the region of 0.2–0.4 cm from the burner nozzle, where the distribution of C_2* is the closest to the nozzle. Researchers have found that the OH* front can be used to characterize the flame front and is closely related to the flame temperature [48]. The flame front represents the region of the most intense combustion reactions, where fuel and oxidizer rapidly undergo rapid chemical reactions and release significant amounts of heat, resulting in the highest rate of temperature change. In the laminar premixed volatile flame on the McKenna burner, the flame front is located approximately 0.26 cm from the nozzle. The region beyond the flame front is defined as the post-flame region, where the reaction rate decreases, and the excited-state radicals are largely quenched.

Fig. 3 demonstrates that volatile components significantly influence the peak intensities of radical spectra in flames. Specifically, the intensities of OH* and C_2* exhibit similar trends in response to different volatile components. When the fuel contains H_2 (Case 2 and Case 6), the intensities of both OH* and C_2* are notably enhanced. In contrast, the effect of volatile components on CH* intensity varies; the presence of C_2H_4 (Case 7) leads to a substantial increase in CH* intensity. Additionally, Fig. 3 presents a comparison between the experimental spectral

Table 1
Gas flow rates and component concentrations.

	Basic flame section(L/min)				Multi-component coexisting flame section				
	φ	CH_4	O_2	N_2	CO ppm	H_2 ppm	C_2H_4 ppm	CH_4 ppm	Combustible Carbon Content ppm
Case 1	1	1.29	2.58	9.71	4500	3500	1500	0	7500
Case 2					0	3500	1500	4500	7500
Case 3					4500	0	1500	0	7500
Case 4					4500	3500	0	3000	7500
Case 5					4500	0	0	3000	7500
Case 6					0	3500	0	7500	7500
Case 7					0	0	1500	4500	7500
Case 8					0	0	0	7500	7500

Table 2
Formation and quenching reactions of excited-state radicals [43–47].

	Reactions	A(cm^3/mol.s)	b	Ea(cal/mol)	Ref.
OH* formation reaction	$CH + O_2 <=> OH^* + CO$	1.80×10^{11}	0.0	0.0	[43]
	$O + H + M <=> OH^* + M$	3.63×10^{13}	0.0	0.0	[44]
OH* quenching reaction	$OH^* <=> OH + h\nu$	1.45×10^{6}	0.0	0.0	[44]
	$OH^* + N_2 <=> OH + N_2$	1.08×10^{11}	0.5	−1238	[43]
	$OH^* + O_2 <=> OH + O_2$	2.10×10^{12}	0.5	−482	[43]
	$OH^* + H_2O <=> OH + H_2O$	5.92×10^{12}	0.5	−861	[43]
	$OH^* + H_2 <=> OH + H_2$	2.95×10^{12}	0.5	−444	[43]
	$OH^* + CO_2 <=> OH + CO_2$	2.75×10^{12}	0.5	−968	[43]
	$OH^* + CO <=> OH + CO$	3.23×10^{12}	0.5	−787	[43]
	$OH^* + CH_4 <=> OH + CH_4$	3.36×10^{12}	0.5	−635	[43]
CH* formation reaction	$C_2H + O <=> CH^* + CO$	1.08×10^{13}	0.0	0.0	[46]
	$C_2H + O_2 <=> CH^* + CO_2$	2.17×10^{10}	0.0	0.0	[46]
CH* quenching reaction	$CH^* <=> CH + h\nu$	1.85×10^{6}	0.0	0.0	[45]
	$CH^* + N_2 <=> CH + N_2$	3.03×10^{2}	3.4	−381	[43]
	$CH^* + O_2 <=> CH + O_2$	2.48×10^{2}	2.1	−1720	[43]
	$CH^* + H_2O <=> CH + H_2O$	5.30×10^{13}	0.0	0.0	[43]
	$CH^* + H_2 <=> CH + H_2$	1.47×10^{14}	0.0	1361	[43]
	$CH^* + CO_2 <=> CH + CO_2$	2.40×10^{-1}	4.3	−1694	[43]
	$CH^* + CO <=> CH + CO$	2.44×10^{12}	0.5	0.0	[43]
	$CH^* + CH_4 <=> CH + CH_4$	1.73×10^{13}	0.0	167	[43]
C_2* formation reaction	$C + CH_2 <=> C_2^* + H_2$	4.80×10^{12}	0.0	0.0	[47]
C_2* quenching reaction	$C_2^* <=> C_2 + h\nu$	1.00×10^{7}	0.0	0.0	[47]
	$C_2^* + M <=> C_2 + M$	4.80×10^{13}	0.0	0.0	[47]

results and the simulated predictions of the maximum concentrations of excited-state radicals. The predicted generation trends of excited-state radicals align consistently with the experimentally measured image spectroscopy results.

As shown in Fig. 3, the formation patterns of excited-state radicals exhibit a significant correspondence with those of their precursor species. This relationship indicates that these radicals can be effectively utilized as reliable indicators for identifying and tracking various reaction pathways.

OH* and C_2* have similar formation patterns owing to the reason that OH* is mainly formed by the reaction $CH + O_2 = OH^* + CO$, while C_2* is mainly formed by the reaction $C + CH_2 = C_2^* + H_2$. The precursors of OH* and C_2* are CH and CH_2 respectively, and CH is mainly generated by the dehydrogenation of CH_2 via the reaction $CH_2 + H = CH + H_2$. Therefore, the formation patterns of OH* and C_2* are relatively close to each other. Fig. 3(d) and (f) show the formation of CH_2 and CH under various cases. In Case 2 and Case 6, the presence of H_2 significantly increases the production of CH_2 and CH, which greatly promotes the formation of OH* and C_2*. Compared to the control group, Case 8, the presence of C_2H_4 in Case 7 slightly inhibits the formation of CH_2 and CH, while CO in Case 5 significantly suppresses the production of CH_2 and CH. The coexistence of multiple components in Case 1, Case 3, and Case 4 also inhibits the formation of CH_2 and CH, thereby reducing the production of OH* and C_2* to varying degrees. In addition, since CH_2 forms earlier than CH, the formation of C_2* is typically closer to the burner nozzle than OH*.

The pathways of CH* formation is $C_2H + O = CH^* + CO$ and $C_2H + O_2 = CH^* + CO_2$, with $C_2H + O = CH^* + CO$ dominating. C_2H is mainly produced by the reaction $C_2H_2 + OH = C_2H + H_2O$. Fig. 3(e) shows the formation of C_2H in different flames. The results indicate that in Case 7, with C_2H_4 in the fuel, it undergoes gradual dehydrogenation to form C_2H_2 and C_2H, which in turn promotes the formation of CH*, leading to a significant increase in CH* intensity.

3.2. Temperature and H_2O generation analysis based on TDLAS

As a final combustion product, changes in H_2O concentration can qualitatively assess the combustion efficiency and completeness of the flame. Flame temperature is a critical parameter in the combustion process. In the experiment, TDLAS technology was used to quantitatively measure the temperature field and H_2O concentration in the flame of volatile light gases, enabling in-situ monitoring of the flame's combustion state. Specifically, DFB lasers with central wavelengths of 1343 nm and 1392 nm were employed to measure H_2O molecules in the combustion field, and the flame temperature was calculated using the two-line method. The absorbances at 7185 and 7444 cm^{-1} are shown in Fig. 4.

The absorption spectrum is based on the Beer-Lambert law, and the absorbance formula is derived through Eq (1).

$$\alpha_\nu = PS(T)x_{H2O}\phi_\nu L = -\ln\left(\frac{I_t}{I_0}\right) \tag{1}$$

In the equation, α_ν represents the absorbance at frequency ν, P is atmospheric pressure, $S(T)$ is the line strength that varies with temperature T, which is obtained by the HITRAN database, x_{abs} is the component concentration, ϕ_ν is the line shape function, L is the absorption path length, I_t is the absorbed light intensity, and I_0 is the incident light intensity.

Voigt line function is used to fit the absorption spectrum and the relative wavenumber range of the DFB laser was calibrated with an F-P etalon prior to the experiment. The integrated absorbance A of the gas is given by Eq (2).

$$A = \int_{\nu_1}^{\nu_2} \alpha_\nu d\nu \tag{2}$$

where ν_1 and ν_2 are the wave number ranges of the absorption peaks.

Utilizing two absorption lines with different responses to temperature enables the measurement of gas temperature, known as the two-line thermometry method. The temperature can be obtained from Eq (3).

$$T = \frac{\frac{hc}{k}\left(E_1'' - E_2''\right)}{\ln\left(\frac{A_1}{A_2}\right) + \ln\left(\frac{S_1(T_0)}{S_2(T_0)}\right) + \left(\frac{hc}{k}\right)\left(\frac{E_2''-E_1''}{T_0}\right)} \tag{3}$$

where h is the Planck constant ($h = 6.626 \times 10^{-34}$ $J \bullet s$), k is the Boltzmann constant ($k = 1.38 \times 10^{-23}$ J/s), c is the speed of light in a vacuum (c = 299792.458 km/s), E_i'' is the lower-state energy level of the absorption line, A_i is the integrated absorbance of the target absorption peak, T_0 is the room temperature (296K), and S_i (T_0) is the line strength at temperature T_0.

The average concentration of the target component (x_{abs}) along the detection path can be calculated as Eq (4):

$$x_{H_2O} = \frac{A}{S(T)LP} \tag{4}$$

By adjusting the displacement platform to change the in-situ measurement position of the TDLAS, temperature-distance curves were

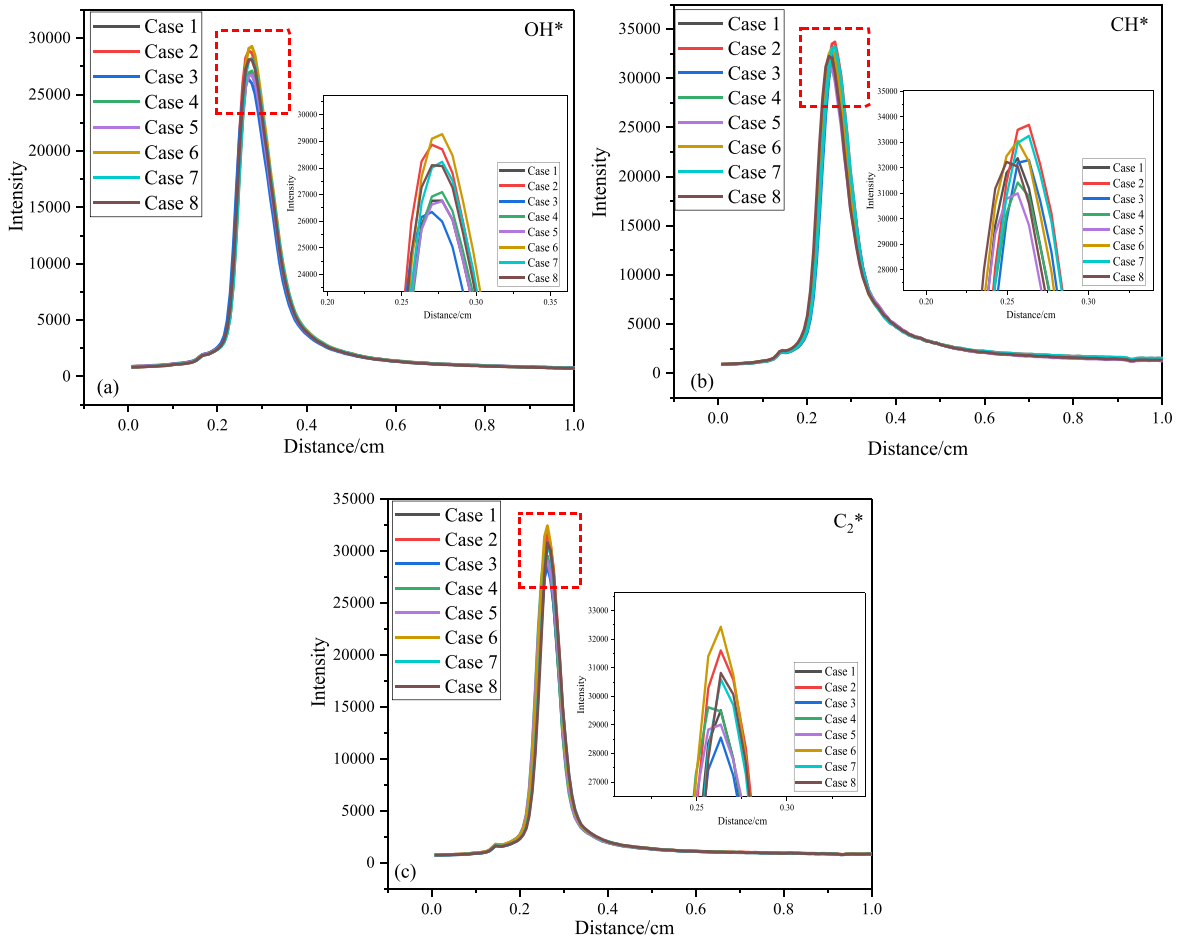

Fig. 2. Imaging spectroscopy of radicals. (a) OH*; (b) CH*; (c) C_2*.

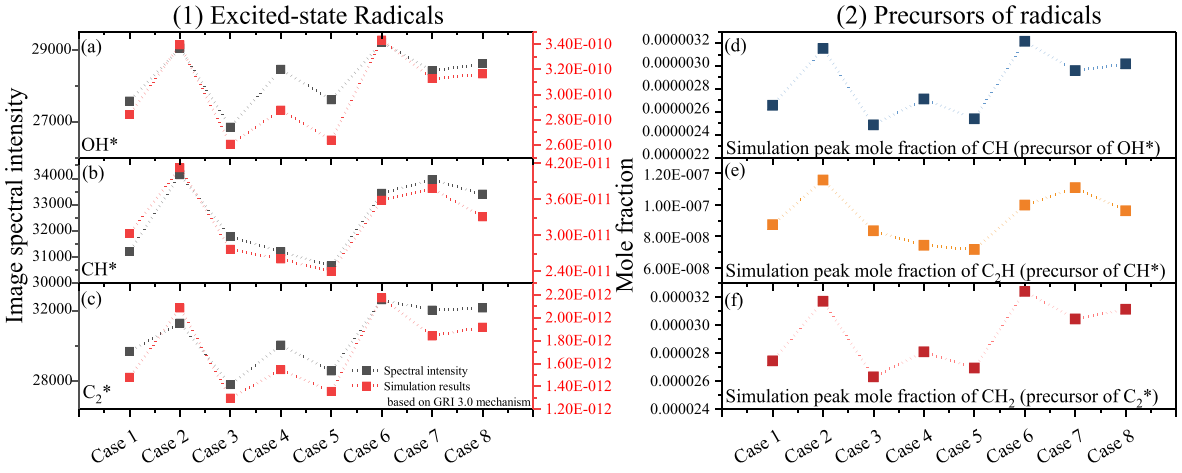

Fig. 3. (1) The image spectral peak intensity of radicals and their kinetic simulation peak concentration; (2) The kinetic simulation peak concentration of radical precursors.

obtained at 0–20 mm above the burner, as shown in Fig. 5. These curves were compared to the simulated combustion field temperatures based on the GRI-Mech 3.0 mechanism. The temperatures measured by TDLAS increase with the distance from the nozzle. Compared to the control group (Case 8), the flame temperatures in Case 6 and Case 2 are higher, while the flame temperatures in the other conditions are lower. The temperature curves measured by TDLAS are qualitatively consistent with the simulation predictions, indicating that the presence of H_2 increases the flame temperature, while the presence of CO decreases it. Combined with the results from the optical spectrum, it is evident that the spectral intensities of OH* and C_2* are closely related to the flame temperature, with their intensities increasing as the flame temperature increases. The spectral intensity of CH* shows a relatively weaker correlation with the flame temperature and is mainly influenced by the formation characteristics of the intermediate product C_2H.

Based on Eq (4), the H_2O concentration can be calculated. As shown

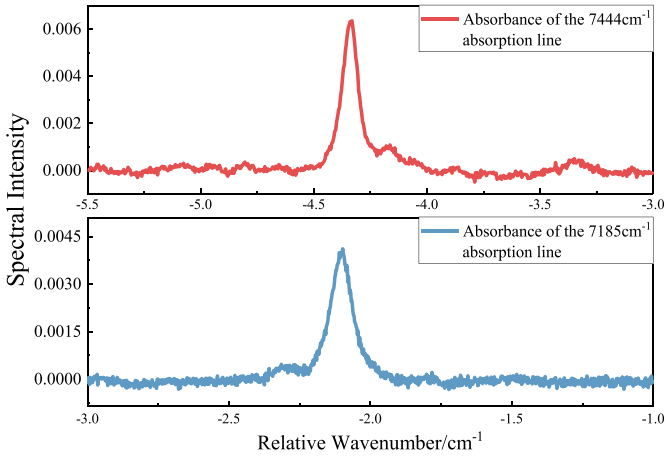

Fig. 4. Absorption of (a) 7185 cm^{-1} and (b) 7444 cm^{-1} absorption line.

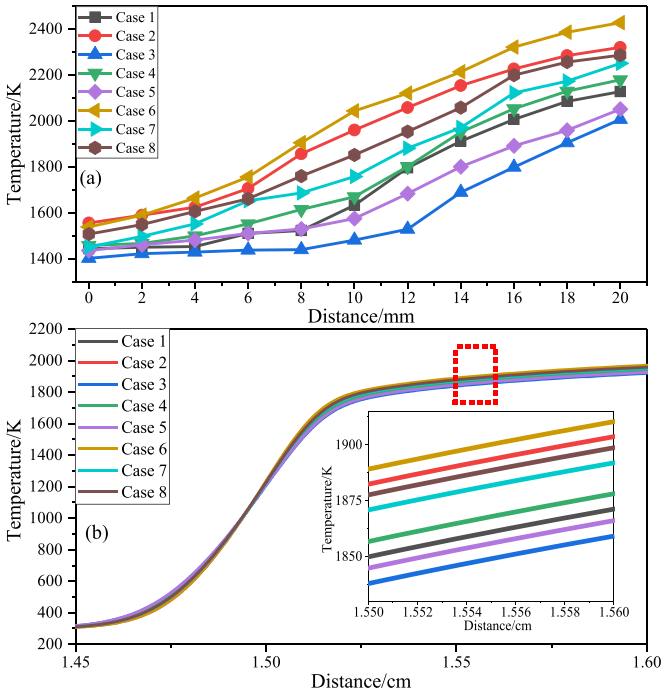

Fig. 5. Flame temperature (a) TDLAS measurement; (b) simulation results.

in Fig. 6, the H_2O concentration in the combustion field increases with distance and reaches about 14–18 vol% at the end of the flame. Compared with Case 8, the H_2O generation is higher in Case 6 and Case 2, which contain H_2 in the fuel, while it decreases to varying degrees in the other cases. The H_2O concentration results measured by TDLAS are in qualitative agreement with the simulation results. This indicates that the presence of CO reduces H_2O production, while the presence of H_2 promotes H_2O generation.

3.3. Analysis of the carbon conversion process based on reaction kinetics

3.3.1. Analysis of carbon conversion efficiency in volatile flames

In the above work, we have measured the spatial and temporal distributions of important intermediate groups (OH*/CH*/C_2*) in the volatile flames by image spectroscopy, as well as the concentration distributions of the final product H_2O and the thermodynamic parameter temperatures by TDLAS, in order to validate the accuracy of the reaction mechanism in terms of the intermediate stage, the final stage,

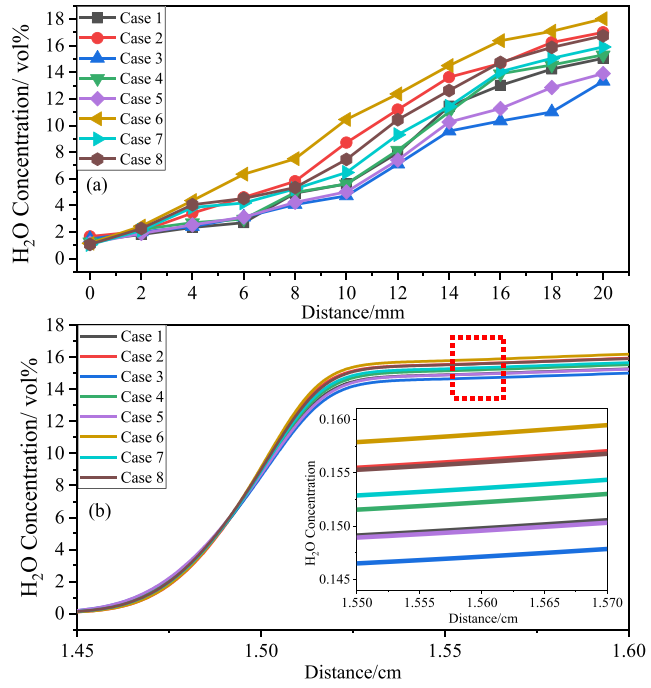

Fig. 6. H_2O concentration (a) TDLAS measurements; (b) simulation results.

and the thermodynamic parameters of the reaction. The results show that the established chemical kinetic model can effectively describe the complex reaction process in multicomponent coexisting volatile flames and provides a data basis for the subsequent simulation calculations.

Based on the chemical reaction kinetics model established, the carbon conversion mechanism was to be further analyzed. CO_2 is the final product of combustion. By monitoring the changes in CO_2 concentration, the efficiency of carbon conversion and the completeness of combustion in the flame can be qualitatively assessed. The CO_2 yield refers to the proportion of carbon in the fuel that is converted to CO_2, as determined by Eq (5).

$$\alpha^{i}_{CO_2} = \frac{c^{i}_{CO_2}}{c^{i}_{Fuel\ C}} \times 100\% \tag{5}$$

where $\alpha^{i}_{CO_2}$ is the CO_2 yield of Case i, $c^{i}_{CO_2}$ is the mole fraction of CO_2 produced by case i, and $c^{i}_{Fuel\ C}$ is the mole fraction of carbon of the reactants in the fuel.

The CO_2 yield gain $A^{i}_{CO_2}$ is the difference in CO_2 yield between each condition and the control group (Case 8), which can be obtained from Eq (6).

$$A^{i}_{CO_2} = \alpha^{i}_{CO_2} - \alpha^{8}_{CO_2} \tag{6}$$

Fig. 7 shows the CO_2 yield and its gain at the flame front and at the end of the post-flame region for each case. Under the condition where the combustible carbon content in the fuel is held consistent, if the CO_2 yield gain is less than zero, it indicates a decreased ability to convert carbon from the fuel into CO_2; if the CO_2 yield gain is greater than zero, it indicates an increased ability to convert carbon from the fuel into CO_2.

Compared to the control group (Case 8), the CO_2 yield gain in Cases 2 and 6, which contain H_2, is lower than zero both at the flame front and at the end of the post-flame region, indicating that these cases inhibit the conversion of carbon from fuel to CO_2. In contrast, the CO_2 yield gain in Case 1, 3, 4, and 5, which contain CO, is higher than zero, indicating that these cases promote the conversion of carbon from fuel to CO_2. CO_2 yield can serve as an effective indicator for quantifying the degree of carbon conversion in volatile combustion, providing a better understanding of the carbon conversion process. The results clearly demonstrate the

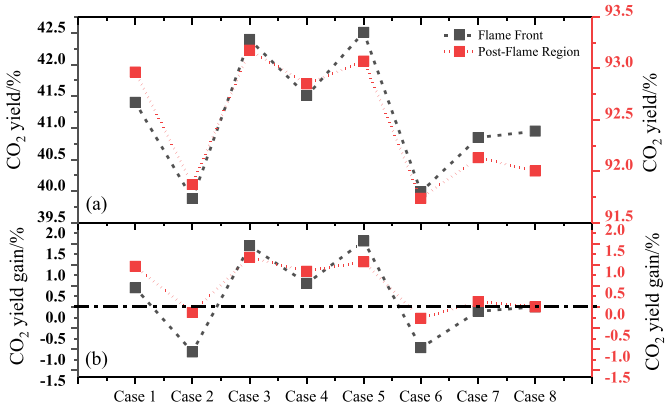

Fig. 7. CO_2 yield and its gain in various cases.

differing effects of various volatile components on carbon conversion. With a consistent combustible carbon content, cases with H_2 show lower CO_2 yield gains, indicating that H_2 inhibits the conversion of carbon to CO_2, while cases with CO enhance this conversion.

To further validate the analysis results, CO_2 concentration in the flue gas at the outlet was measured in real-time using a gas analyzer (Testo 350), which has a measurement resolution of 0.01 vol%. For each case, three 1-min continuous measurements were taken, and the average value was calculated. The measurement results are shown in Fig. 8. The gas analysis revealed that the CO_2 concentration was lowest in Case 2 (with H_2 and C_2H_4) and Case 6 (with H_2 only), at 7.95 vol% and 7.85 vol %, respectively. In contrast, in cases containing CO (Case 1, 3, 4, and 5), the CO_2 concentration exceeded 9 vol%. In the control group (Case 8), the outlet CO_2 concentration was 8.35 vol%. The trend is consistent with the predictions from the chemical kinetics simulation. This comparative validation allows for a more accurate assessment of the chemical kinetics model's predictive performance, ensuring consistency between theoretical predictions and experimental measurements.

3.3.2. *Carbon conversion pathway analysis*

By analyzing the yield of CO_2, it can be found that the different components of the volatile fraction have different effects on elemental carbon conversion, either promoting or inhibiting the process. In addition, the interactions between components may also have a synergistic effect on carbon conversion. The combustion process involves a variety

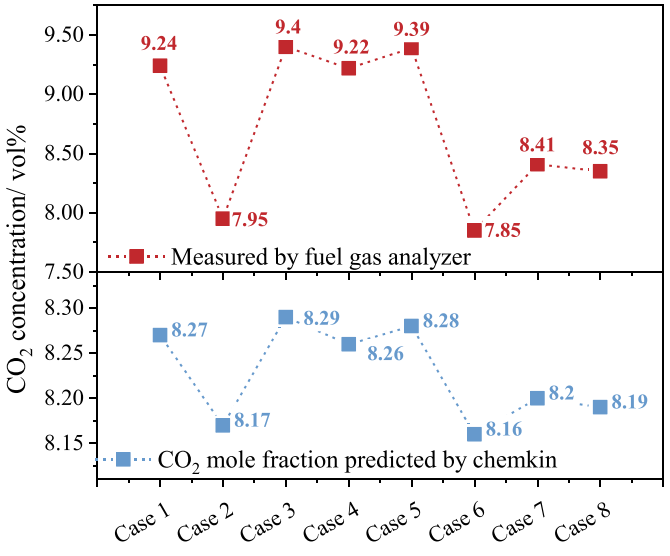

Fig. 8. CO_2 concentration in the flue gas measured by gas analyzer and its mole fraction predicted by chemkin.

of radicals and complex chemical reactions, so identifying the elemental reactions that have a significant impact on CO_2 generation is essential to understanding the mechanism of carbon conversion. To identify the elementary reactions that have the greatest impact on carbon conversion, a sensitivity analysis was performed on the final product CO_2 and examined changes in these key elementary reactions under different reaction conditions. A larger sensitivity coefficient indicates that the elementary reaction has a greater influence on the carbon conversion process.

As shown in Fig. 9, the top ten elementary reactions with positive CO_2 sensitivity coefficients can be categorized into three types. The first type includes elementary reactions in the main reaction chain, such as R53 $H + CH_4 = CH_3 + H_2$, R58 $H + CH_2O = HCO + H_2$, R166 $HCO + H_2O = H + CO + H_2O$, and R99 $OH + CO = H + CO_2$. The second type consists of the branch elementary reactions in the side chain, including R142 $CH_2^* + N_2 = CH_2 + N_2$, R290 $CH_2 + O_2 = 2H + CO_2$ and R284 $O + CH_3 = H + H_2 + CO$. The third type involves the formation and consumption of the key oxidizer OH, including R38 $H + O_2 = O + OH$, R86 $2OH = O + H_2O$, and R3 $O + H_2 = H + OH$.

Fig. 10 shows the reaction pathways of carbon conversion and the distribution of key elementary reactions in the volatile flame. By analyzing the overall reaction pathways in the volatile flame, it can be found that the elementary reactions that have the greatest impact on CO_2 production are present throughout the elemental carbon conversion process. The carbon conversion pathways in the volatile flame primarily include: (1) CH_4 is dehydrogenated to form CH_3, which is further oxidized to CH_2O, then to HCO, and finally to CO and CO_2; (2) CH_4 is dehydrogenated to CH_3, which reacts with OH to form CH_2^*, then further transforms into CH_2 and CH, which are oxidized to CH_2O and HCO, and finally convert to CO and CO_2; (3) CH_3 is directly oxidized to CO, which is subsequently oxidized to CO_2; (4) two CH_3 molecules combine to form C_2H_6, which then undergoes successive dehydrogenation to form C_2H_5, C_2H_4, C_2H_3, and C_2H_2, ultimately oxidizing to CO and CO_2. Reactions such as R53, R58, R166, and R99 are part of the main chain of the carbon conversion reaction pathway ($CH_4 \rightarrow CH_3 \rightarrow CH_2O \rightarrow HCO \rightarrow CO \rightarrow CO_2$), while R284, R142, and R290 are branch reactions.

Based on the sensitivity analysis of CO_2 formation and the analysis of the carbon conversion pathways, it is clear that R99 $OH + CO = H + CO_2$ is the elementary reaction where CO is directly converted to CO_2, with the highest sensitivity coefficient, making it the most critical reaction for CO_2 formation. Reactions R38 $H + O_2 = O + OH$, R3 $O + H_2 = H + OH$, and R86 $2OH = O + H_2O$ either produce or consume the key oxidizer OH, thus promoting CO_2 formation in the R99 reaction. The branch reactions R290 $CH_2 + O_2 = 2H + CO_2$ and R142 $CH_2^* + N_2 = CH_2 + N_2$ are also crucial for CO_2 formation. CH_2 is an important intermediate product in oxidation branch reactions, formed from the excited state CH_2^*, and by consuming CH_2, CO_2 is directly produced, making this the second most

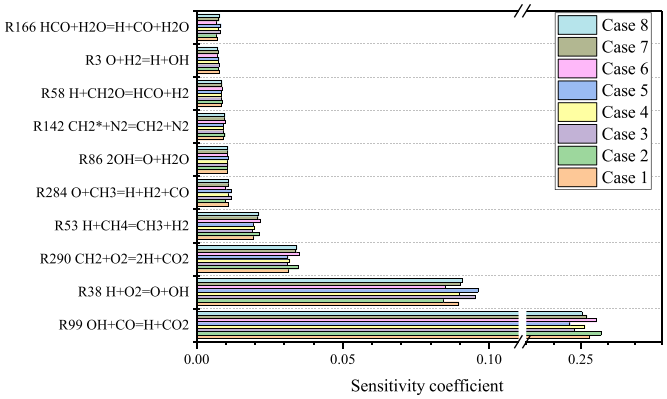

Fig. 9. Results of CO_2 sensitivity analysis.

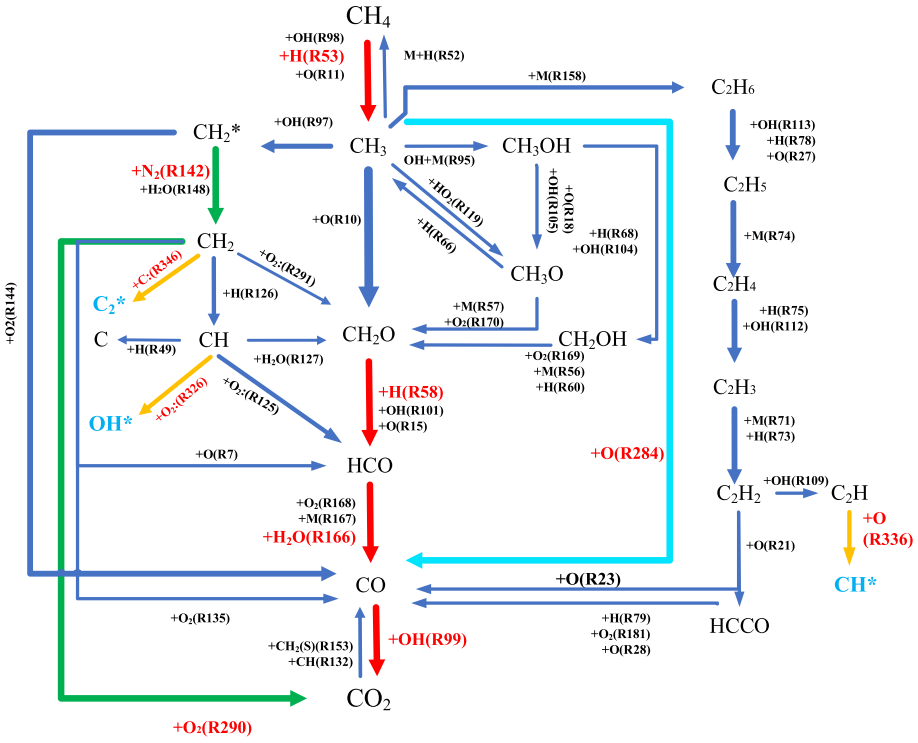

Fig. 10. Carbon conversion reaction pathways and the key elementary reactions.

significant pathway for CO_2 formation after R99. Additionally, the main-chain oxidation reactions R53 H + CH_4=CH_3+H_2, R58 H + CH_2O=HCO + H_2 and R166 HCO + H_2O=H + CO + H_2O significantly contribute to CO_2 formation. Another branch reaction, R284 O + CH_3=H + H_2+CO, promotes CO_2 formation by consuming CH_3 to generate CO, further facilitating the process.

In addition, based on the carbon transformation pathway analysis, the formation of C_2* is primarily attributed to the excitation of CH_2, while OH* is mainly formed due to the excitation of CH. Since the formation of CH_2 and CH follows the same reaction pathway, the characteristics of the formation of these two excited-state radicals are similar. On the other hand, CH* is primarily generated from the excitation of C_2H, with its formation process influenced by the C_2 intermediate products in flames. These radicals represent the reaction pathways of different intermediate products in the volatile flame. Specifically, C_2* and OH* reflect the pathway involving CH_2 and CH, while CH* reflects the pathway of C_2 intermediates.

3.4. ROP analysis of flame fronts and post-flame region

Through sensitivity analysis of CO_2 formation, we can identify the elementary reactions that have the greatest impact on carbon conversion among the complex combustion reactions. The analysis of these key elementary reactions helps to simplify the combustion process and provides a qualitative understanding of the overall carbon conversion mechanism. Furthermore, by performing ROP analysis and comparing the rate changes of each reaction in different cases, the specific effects of various volatile components on carbon conversion can be revealed.

Fig. 11 shows the reaction rates in the flame front and post-flame region for different cases. There are significant differences in ROP gains between the two regions. In the flame front region, where the temperature changes most drastically, its impact on reaction rates is significant. Case 6, which contains H_2, exhibited the highest flame temperature, resulting in notable gains across various elementary reactions, especially R38, R53, R284, R86, and R58. When H_2 coexisted with C_2H_4 (Case 2), the flame temperature was also elevated, leading to

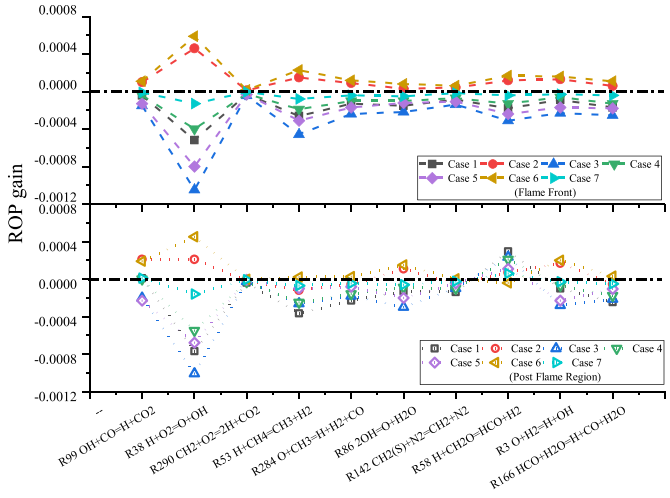

Fig. 11. The ROP gain of the elementary reaction.

significant rate increases in several reactions. In contrast, the presence of CO (Case 1, Case 3, Case 4, and Case 5) caused a noticeable decrease in flame temperature, leading to varying degrees of reduction in reaction rates. When only C_2H_4 was present (Case 7), it slightly suppressed the reaction rates. In the post-flame region, the flame temperature becomes more stable, reducing its impact on reaction rates. Instead, the influence of fuel components on reaction rates becomes significantly greater, making the chemical composition of the fuel a key factor in carbon conversion rates in this area. In Case 2 and Case 6, the rate gains for these elementary reactions have decreased, particularly for reactions R38, R53, R284, and R58. Meanwhile, in other cases, the reaction rates for R58, R53, and similar reactions have shown varying degrees of increase.

The above analysis indicates that, the rates of elementary reactions are affected by both the flame temperature and the chemical

composition of the fuel. In the flame front region where temperature fluctuations are the largest, the flame temperature plays a crucial role in determining the reaction rates. In the post-flame region, where the temperature stabilizes, the effect of fuel composition on the reaction rate dominates. Notably, the reaction R290 ($CH_2 + O_2 = 2H + CO_2$) is the least sensitive to temperature and fuel composition, resulting in negligible changes in ROP gain.

3.5. Global carbon conversion pathway analysis for multi-component coexistence flames

The reaction rates in both the flame front and post-flame regions are jointly influenced by fuel composition and flame temperature. To accurately construct the carbon conversion reaction pathways and fully understand how variations in fuel composition affect reaction rates and their impact on the carbon conversion pathways, it is essential to perform the global carbon conversion pathway analysis of key elementary reactions across the full computational domain. The overall carbon conversion pathways and the pathway proportions of key elementary reactions are shown in Fig. 12, where the numbers indicate the proportion of reactant *A* consumed by elementary reaction *i* relative to its total consumption. The calculation method is given in Eq (7).

$$\varphi_A^i = \frac{\int_0^L ROP_i^i dl}{\sum_i^n \left(\int_0^L ROP_i^i dl \right)} \times 100\% \tag{7}$$

where φ_A^i is the pathway proportions of key elementary reaction *i*; $\int_0^L ROP_i^i dl$ is the ROP integral value of the reaction *i* in the computational domain; $\sum_i^n \left(\int_0^L ROP_i^i dl \right)$ is the sum of ROP integrals of all reactions that consume reactant *A*.

By comparing the pathway proportions across different cases in the full computational domain, the conversion ratios of these key elementary reactions in the pathway can be analyzed, revealing the pathway tendencies in the carbon conversion process and providing a deeper understanding of how different fuel components specifically affect carbon conversion and the formation of the final product CO_2.

The gains in pathway proportion for key elementary reactions across the full computational domain, in cases where only a single volatile component exists in fuel, are shown in Fig. 13. When CO is the only volatile component present in the fuel (Case 5), it significantly increases the pathway proportions of R290 and R142, while decreasing the pathway proportions of R53, R58, and R166. This indicates that the presence of CO significantly promotes the conversion ratios in the reaction branches $CH_2^* \rightarrow CH_2$ and $CH_2 \rightarrow CO_2$, while weakening the conversions in the main chain reactions $CH_4 \rightarrow CH_3$, $CH_2O \rightarrow HCO$, and

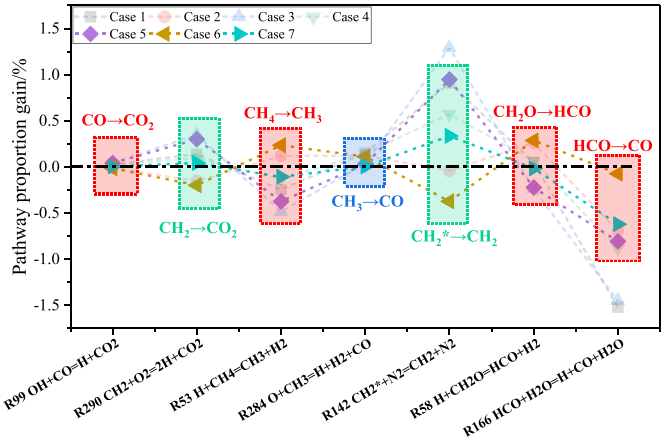

Fig. 13. The gains in pathway proportions for the key elementary reactions across the computational domain in cases with only a single volatile component in fuel.

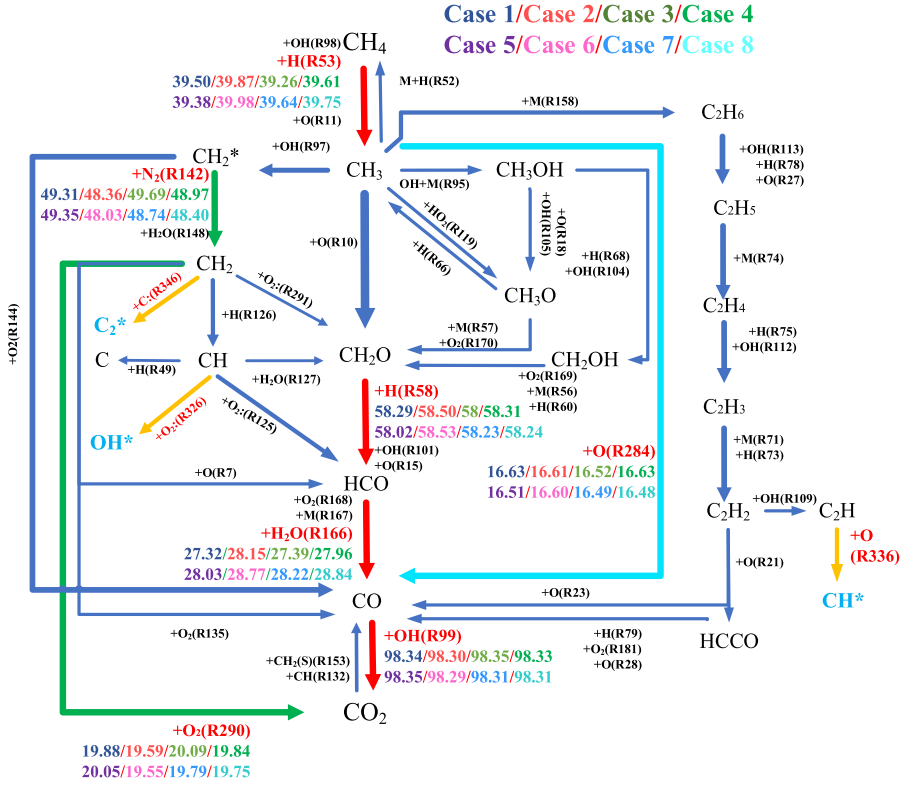

Fig. 12. Combustion reaction pathways of various volatile component gas flames.

HCO → CO. Consequently, it promotes the conversion of carbon elements from the fuel to CO_2, given a consistent combustible carbon content. When H_2 is the only volatile gas in the fuel (Case 6), the pathway proportions of R99, R290, R142, and R166 are suppressed to varying degrees, while the pathway proportions of R53 and R58 show a slight increase. This indicates that the presence of H_2 reduces the proportions of the pathways for the main chain reactions CO → CO_2 and HCO → CO, as well as the branch reactions CH_2* → CH_2 and CH_2→ CO_2, while slightly increasing the proportions of the pathway for CH_4 → CH_3 and CH_2O → HCO. Consequently, the conversion of fuel carbon to the final product CO_2 is reduced, while the combustible carbon content of the fuel remains constant. When only C_2H_4 is present (Case 7), the pathway proportions of R290 and R142 increase slightly, while the pathway proportions of R53 and R166 decrease. This suggests that the presence of C_2H_4 slightly increases the path proportions for the branch reactions CH_2* → CH_2 and CH_2→ CO_2, while suppressing the pathway proportions for the main chain reactions CH_4→ CH_3 and HCO → CO.

In cases where multiple components coexist in the fuel, the gains in pathway proportions become more complex. When various volatile components coexist, the gains in pathway proportions are influenced not only by each individual component but also by additional synergistic effects. The pathway proportions for multiple component coexistence are given by Eq (8).

$$\Delta\gamma_{Ri}^{a+b} = \left(\Delta\gamma_{Ri}^{a} + \Delta\gamma_{Ri}^{b}\right) + R_{Ri}^{a+b} \tag{8}$$

where $\Delta\gamma_{Ri}^{a+b}$ represents the gain in pathway proportion for reaction R_i when components ***a*** and ***b*** coexist, $\Delta\gamma_{Ri}^{a}$ represents the gain in pathway proportion when component ***a*** is present alone, $\Delta\gamma_{Ri}^{b}$ represents the gain in pathway proportion when component ***b*** is present alone, and R_{Ri}^{a+b} represents the synergistic change in pathway proportion. Therefore, the synergistic change in pathway proportion can be obtained by Eq (9).

$$R_{Ri}^{a+b} = \Delta\gamma_{Ri}^{a+b} - \left(\Delta\gamma_{Ri}^{a} + \Delta\gamma_{Ri}^{b}\right) \tag{9}$$

when R_{Ri}^{a+b} is greater than zero, it indicates a synergistic promotion effect when components ***a*** and ***b*** coexist. If R_{Ri}^{a+b} equals zero, it indicates that the coexistence of components ***a*** and ***b*** results in a simple additive effect. If R_{Ri}^{a+b} is less than zero, it indicates a synergistic suppression effect between components *a* and *b* when they coexist.

In this study, we focus on analyzing Case 2, where H_2 and C_2H_4 coexist as volatile components in the fuel. Analyzing this specific case provides insights into their overall effects and synergistic gains on pathway proportion. For the other multicomponent coexistence cases, the analytical methods and approaches used are consistent with those applied to Case 2. Therefore, further elaboration on these cases will be omitted to maintain focus and clarity.

In Case 2, where H_2 and C_2H_4 coexist in the fuel, the pathway proportion gains are shown in Fig. 14. Compared to the case where only H_2 is present (Case 6), Case 2 decreases the pathway proportion gains of CH_4→CH_3 (R53) and CH_2O→HCO (R58), weakens the inhibitory effects on the pathway proportions of CH_2*→CH_2 (R142) and CH_2→CO_2 (R290), but intensifies the inhibitory effect on the pathway proportion of HCO→CO (R166). In terms of the overall effect, Case 2 similarly inhibits the conversion of carbon from the fuel into CO_2.

In Case 2, the pathway proportion gains for key elementary reactions are not solely determined by the individual effects of H_2 and C_2H_4 but are also influenced by synergistic effects, as shown in Fig. 15. The reduction in pathway proportion gains for CH_4→CH_3 (R53) and CH_2O→HCO (R58) in Case 2 results from the combined effect of the promoting effect of H_2 and the inhibiting effect of C_2H_4, along with additional synergistic suppression when H_2 and C_2H_4 coexist. The weakening of the pathway proportion inhibition for CH_2 *→CH_2 (R142) and CH_2→CO_2 (R290) is due not only to the suppression by H2 and the promotion by C_2H_4 but also to the synergistic promotion effect for R290

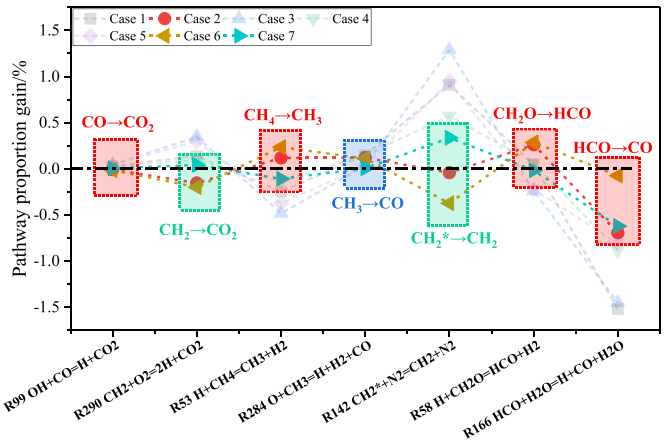

Fig. 14. The gains in pathway proportions for the key elementary reactions across the computational domain in Case 2, 6 and 7.

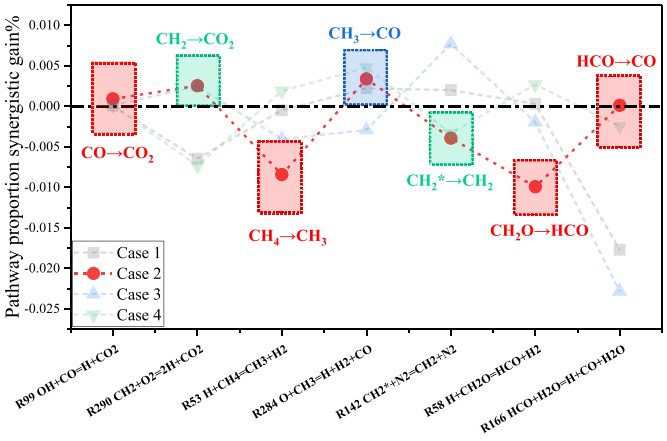

Fig. 15. Synergistic effects on pathway proportion gains for key elementary reactions in Case 2.

and synergistic suppression for R142. Although Case 2 intensified the inhibition of the pathway proportion for HCO→CO (R166), the synergistic effect was nearly zero, indicating that the inhibition of R166 is simply the additive effect of H_2 and C_2H_4.

The same method was used to analyze other multicomponent coexistence cases, calculating the synergistic variations for each case and presenting these changes in Fig. 16. It reveals the synergistic effects of key elementary reactions under different multicomponent coexistence cases. As shown in Fig. 16, the synergistic effects in multicomponent combustion are highly complex, mainly in two aspects. First, each volatile component affects carbon conversion in a specific manner, and in multicomponent coexistence cases, the overall effect on carbon conversion is a result of the combined impacts of the individual components, with different combinations producing varying effects. Second, even within the same multicomponent flame, the synergistic effects on different elementary reactions vary, with some reactions exhibiting synergistic promotion, others facing synergistic inhibition, or simply showing additive effects. Therefore, to accurately reveal the complexity of synergistic changes, it is essential to conduct a detailed analysis of the reaction mechanisms in each case, clarifying the variations in carbon conversion pathways and the specific synergistic effects between elementary reactions in each multicomponent system.

In summary, the variation in volatile fuel components significantly affects the pathway proportions of key elementary reactions and impacts the conversion of carbon from fuel to CO_2. When there is only one volatile component in the fuel, the presence of CO and C_2H_4 primarily

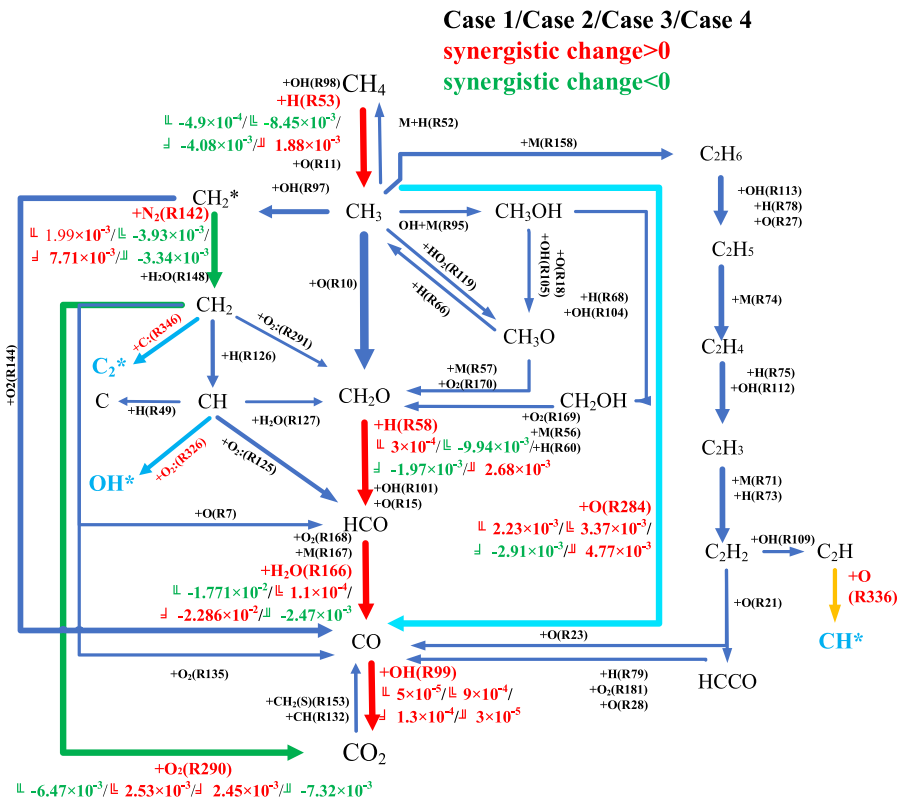

Fig. 16. The synergistic effects of key elementary reactions under different multicomponent coexistence cases.

promotes the conversion of carbon in the fuel to CO_2 by increasing the pathway proportions of the branched reactions involving CH_2* and CH_2. In contrast, the presence of H_2 inhibits the conversion of carbon to CO_2 by reducing the pathway proportions of both the main-chain reactions involving HCO and CO, as well as the branched reactions involving CH_2* and CH_2. When multiple volatile components coexist in flames, the pathway proportion gains $\Delta\gamma_{Ri}^{a+b}$ are influenced not only by pathway proportion gains in individual components $\Delta\gamma_{Ri}^{a}$ and $\Delta\gamma_{Ri}^{b}$, but also by complex synergistic effects R_{Ri}^{a+b}. It is crucial to conduct a detailed analysis of carbon conversion pathways and the synergistic effects of specific elementary reactions to better reveal the carbon conversion mechanisms in multi-component flames.

4. Conclusion

This study has systematically revealed the carbon conversion pathways in volatile flames and the synergistic effects of co-combustion of various volatile components on these pathways. Multi-spectral diagnostic techniques (imaging spectroscopy and TDLAS) were utilized to obtain the spatial distribution characteristics of radical OH*, CH*, and C_2* spectral intensities, H_2O concentration, and flame temperature in CH_4/CO/C_2H_4/H_2/air laminar premixed flames. The accuracy of the established chemical kinetic model was validated from the perspectives of intermediate reaction products, final products, and thermodynamic parameters. Furthermore, a more comprehensive kinetic model of the volatile flame chemical reaction was established, based on which the key elementary reactions were illustrated, the formation characteristics of the relevant components were analyzed, and the synergistic effect of the carbon conversion pathway were revealed. Experimental and kinetic simulation results indicate that.

(1) C_2*, OH*, and CH* are generated from CH_2, CH, and C_2H, respectively, and the spectral patterns of these excited radicals are consistent with the formation patterns of their precursors. The presence of H_2 in the volatile flame promotes the formation of CH_2 and CH, thereby enhancing the formation of C_2* and OH*. The presence of C_2H_4 promotes the formation of C_2H, which enhances the formation of CH*.

(2) The presence of H_2 in flame enhances the generation of H_2O and increases the flame temperature, while CO reduces both H_2O generation and the flame temperature. Both the flame temperature and the composition of volatile components influence the reaction rates of the elementary reactions.

(3) The key elementary reactions for the generation of the final product CO_2 are present throughout the entire carbon conversion process. With the combustible carbon content in the fuel kept consistent, H_2 mainly inhibits the conversion of carbon from the fuel to CO_2 by reducing the pathway proportions of both main chain reactions of HCO and CO, and branch reactions of CH_2* and CH_2. In contrast, CO and C_2H_4 promote the conversion of carbon to CO_2 by increasing the pathway proportions of branch reactions of CH_2* and CH_2.

(4) When multiple volatile components coexist in flame, the gain in pathway proportions is not only influenced by the individual effects of each component, but also the complex synergistic effects. The synergistic effects on different elementary reactions vary greatly and may appear as synergistic promotion, synergistic inhibition, or simple additive effects.

This study clarifies the carbon conversion synergistic patterns in multi-component flames by comparing the effects of individual volatile components and their coexistence, providing a scientific basis for understanding the chemical kinetic mechanisms of volatile combustion.

CRediT authorship contribution statement

Xiao Lin: Writing – review & editing, Writing – original draft, Visualization, Validation, Software, Methodology, Investigation, Formal analysis, Data curation, Conceptualization. **Meirong Dong:** Writing – review & editing, Writing – original draft, Supervision, Methodology, Funding acquisition, Formal analysis, Conceptualization. **Gangfu Rao:** Investigation, Formal analysis, Conceptualization. **Wei Nie:** Resources, Methodology, Investigation, Funding acquisition. **Guangchi Zhou:** Methodology, Formal analysis, Data curation. **Jidong Lu:** Writing – review & editing, Methodology, Conceptualization.

Notes

The authors declare no competing financial interest.

Data availability

The data that has been used is confidential.

Funding

The research was supported by the National Natural Science Foundation of China [No. 51976064, 52376107, 62105104]; the Guangdong Basic and Applied Basic Research Foundation [2022A1515010709]; and the Fundamental Research Funds for the Central Universities (2022ZFJH004).

Declaration of competing interest

The authors declare that they have no known competing financial interests or personal relationships that could have appeared to influence the work reported in this paper.

Acknowledgement

The research acknowledges the support from the Guangdong Province Key Laboratory of Efficient and Clean Energy Utilization (2013A061401005).

References

[1] T. Wang, C. Li, B. Zhou, Y. Zhang, M. Zhang, H. Yang, Z. Wang, Experimental investigation of thermal effect in coal pyrolysis process, J. Fuel Process. Technol. 200 (2020) 106269, https://doi.org/10.1016/j.fuproc.2019.106269.
[2] R. Knappstein, G. Kuenne, A. Ketelheun, J. Köser, L. Becker, S. Heuer, M. Schiemann, V. Scherer, A. Dreizler, A. Sadiki, J. Janicka, Devolatilization and volatiles reaction of individual coal particles in the context of FGM tabulated chemistry, J. Combust. Flame. 169 (2016) 72–84, https://doi.org/10.1016/j.combustflame.2016.04.014.
[3] J. Riaza, J. Gibbins, H. Chalmers, Ignition and combustion of single particles of coal and biomass, J. Fuel. 15 (2017) 650–655, https://doi.org/10.1016/j.fuel.2017.04.011.
[4] N.T. Weiland, N.C. Means, B.D. Morreale, Product distributions from isothermal co-pyrolysis of coal and biomass, J. Fuel 94 (2012) 563–570, https://doi.org/10.1016/j.fuel.2011.10.046.
[5] Y. Jianga, P. Zong, B. Tian, F. Xu, Y. Tiana, Y. Qiao, J. Zhang, Pyrolysis behaviors and product distribution of Shenmu coal at high heating rate: a study using TG-FTIR and Py-GC/MS, J. Energ. Convers. Manage. 179 (2019) 72–80, https://doi.org/10.1016/j.enconman.2018.10.049.
[6] X. Wen, H. Wang, Y. Luo, K. Luo, J. Fan, Numerical investigation of the effects of volatile matter composition and chemical reaction mechanism on pulverized coal combustion characteristics, J. Fuel. 210 (2017) 695–704, https://doi.org/10.1016/j.fuel.2017.08.115.
[7] B. Ye, R. Zhang, J. Cao, K. Lei, D. Liu, The study of co-combustion characteristics of coal and microalgae by single particle combustion and TGA methods, J. J. Energy Inst. 93 (2020) 508–517, https://doi.org/10.1016/j.joei.2019.07.001.
[8] R. Khatami, Y.A. Levendis, An overview of coal rank influence on ignition and combustion phenomena at the particle level, J. Combust. Flame. 164 (2016) 22–34, https://doi.org/10.1016/j.combustflame.2015.10.031.
[9] L. Shan, M. Kong, T.D. Bennet, A.C. Sarroza, C. Eastwick, D. Sun, G. Lu, Y. Yan, H. Liu, Studies on combustion behaviours of single biomass particles using a visualization method, J. Biomass Bioenerg. 109 (2018) 54–60, https://doi.org/10.1016/j.biombioe.2017.12.008.
[10] H. Lee, S. Choi, Volatile flame visualization of single pulverized fuel particles, J. Powder Technol. 333 (2018) 353–363, https://doi.org/10.1016/j.powtec.2018.04.048.
[11] J. Zhu, X. Liu, Y. Xu, J. Xu, H. Wang, K. Zhang, X. Cheng, D. Yu, Probing into volatile combustion flame and particulate formation behavior during the coal and ammonia Co-firing process, J. Energ. Fuel. 36 (2022) 9347–9356, https://doi.org/10.1021/acs.energyfuels.2c01450.
[12] L. Selle, T. Poinsot, B. Ferret, Experimental and numerical study of the accuracy of flame-speed measurements for methane/air combustion in a slot burner, J. Combust. Flame. 158 (2011) 146–154, https://doi.org/10.1016/j.combustflame.2010.08.003.
[13] S. Zheng, Y. Yang, X. Li, H. Liu, W. Yan, R. Sui, Q. Lu, Temperature and emissivity measurements from combustion of pine wood, rice husk and fir wood using flame emission spectrum, J. Fuel Process. Technol. 204 (2020) 106423, https://doi.org/10.1016/j.fuproc.2020.106423.
[14] J. Peng, Z. Cao, X. Yu, H. Qi, R. Sun, Y. Yu, G. Chang, L. Gao, W. Zhu, Z. Zhang, Oscillation characterization of volatile combustion of single coal particles with multi-species optical diagnostic techniques, J. Fuel. 282 (2020) 118845, https://doi.org/10.1016/j.fuel.2020.118845.
[15] H. Qi, R. Sun, J. Peng, B. Yan, Z. Cao, Y. Yu, G. Chang, X. Ren, S. Ding, Experimental study on ignition and combustion characteristics of pyrolyzed char in an O_2-enriched atmosphere with multiple optical diagnostic techniques, J. Energ. Fuel. 33 (2019) 5682–5694, https://doi.org/10.1021/acs.energyfuels.9b00658.
[16] J. Kojima, Y. Ikeda, T. Nakajima, Basic aspects of OH(A), CH(A), and C2(d) chemiluminescence in the reaction zone of laminar methane-air premixed flames, J. Combust. Flame. 140 (2005) 34–45, https://doi.org/10.1016/j.combustflame.2004.10.002.
[17] K. Wang, F. Li, Y. Wu, X. Yu, Quantitative measurements of chemiluminescence in a laminar methane–air premixed flame and comparison to numerical methods, J. Energ. Fuel. 32 (2018) 5536–5543, https://doi.org/10.1021/acs.energyfuels.7b03484.
[18] Q. Wu, F. Wang, M. Li, J. Yan, K. Cen, Simultaneous in-situ measurement of soot volume fraction, H_2O concentration, and temperature in an ethylene/air premixed flame using tunable diode laser absorption spectroscopy, J. Combust. Sci. Technol. 189 (2017) 1571–1590, https://doi.org/10.1080/00102202.2017.1308358.
[19] A. Sepman, Y. Ögren, Z. Qu, H. Wiinikka, F.M. Schmidt, Real-time in situ multi-parameter TDLAS sensing in the reactor core of an entrained-flow biomass gasifier, J. P. Combust. Inst. 36 (2017) 4541–4548, https://doi.org/10.1016/j.proci.2016.07.011.
[20] M.M. Sentko, S. Schulz, B. Stelzner, C. Anderlohr, M. Vicari, D. Trimis, Determination of temperature and water-concentration in fuel-rich oxy-fuel methane flames applying TDLAS, J. Combust. Flame. 214 (2020) 336–345, https://doi.org/10.1016/j.combustflame.2020.01.003.
[21] X. Liu, Y. Ma, Tunable diode laser absorption spectroscopy based temperature measurement with a single diode laser near 1.4 μm, J. Sensors-Basel. 22 (2002) 1–11, https://doi.org/10.3390/s22166095.
[22] R.M. Kumar, S. Adhikari, B. Emerson, C.A. Fugger, T. Lieuwen, Blowoff of bluff body flames: transient dynamics and three dimensional effects, J. Combust. Flame. 244 (2022) 112245, https://doi.org/10.1016/j.combustflame.2022.112245.
[23] R.M. Kumar, S. Adhikari, O. Bibik, B.L. Emerson, C.A. Fugger, T.C. Lieuwen, Simultaneous multiple laser beam intensity profile correction and its application to a vitiated bluff body combustor field, J. Appl Opt. 61 (2022) 532–539, https://doi.org/10.1364/AO.440708.
[24] O. Chaib, Y. Zheng, S. Hochgreb, I. Boxx, Hybrid algorithm for the detection of turbulent flame fronts, J. Exp. Fluids. 64 (2023) 104, https://doi.org/10.1007/s00348-023-03651-6.
[25] M. Tanahashi, S. Murakami, G. Choi, Y. Fukuchi, T. Miyauchi, Simultaneous CH–OH PLIF and stereoscopic PIV measurements of turbulent premixed flames, J. P. Combust. Inst. 30 (2005) 1665–1672, https://doi.org/10.1016/j.proci.2004.08.270.
[26] G. Rao, M. Dong, W. Nie, X. Lin, Y. Liang, J. Lu, Study on the mechanism of nitrogen conversion in NH3-doped methane premixed flame based on multi-spectral analysis methods, J. J. Energy Inst. 111 (2023) 101437, https://doi.org/10.1016/j.joei.2023.101437.
[27] M. Taniguchi, T. Kozuma, Y. Takashima, T. Tsumura, Development of a coal combustion model compliant with the CHEMKIN format for use in Co-firing analysis with hydrogen and low-carbon fuels, J. Energ. Fuel. 37 (2023) 657–666, https://doi.org/10.1021/acs.energyfuels.2c03376.
[28] M. Xia, D. Zabrodiec, P. Scouflaire, B. Fiorina, N. Darabiha, Experimental and numerical studies of pulverized coal devolatilization and oxidation in strained methane/air flames, J. P. Combust. Inst. 36 (2017) 2123–2130, https://doi.org/10.1016/j.proci.2016.07.080.
[29] D. Wang, C. Ji, S. Wang, H. Meng, Z. Wang, J. Yang, Further understanding the premixed methane/hydrogen/air combustion by global reaction pathway analysis and sensitivity analysis, J. Fuel. 259 (2020) 116190, https://doi.org/10.1016/j.fuel.2019.116190.
[30] K. Zhang, G. Hu, S. Liao, Z. Zuo, H. Li, Q. Cheng, C. Xiang, Numerical study on the effects of oxygen enrichment on methane/air flames, J. Fuel. 176 (2016) 93–101, https://doi.org/10.1016/j.fuel.2016.02.064.
[31] S. Prucker, W. Meier, W. Stricker, A flat flame burner as calibration source for combustion research: temperatures and species concentrations of premixed H_2/air flames, J. Rev. Sci. Instrum. 65 (1994) 2908–2911, https://doi.org/10.1063/1.1144637.

[32] L. Jiang, C. Gu, G. Zhou, F. Li, Q. Wang, Cellular instabilities of n-butane/air flat flames probing by PLIF-OH and PLIF-CH2O laser diagnosis, J. Exp. Therm. Fluid Sci. 118 (2020) 110155, https://doi.org/10.1016/j.expthermflusci.2020.110155.
[33] D. Alviso, M. Mendieta, J. Molina, J.C. Rolón, Flame imaging reconstruction method using high resolution spectral data of OH, CH and C_2 radicals, J. Int. J. Therm. Sci. 121 (2017) 228–236, https://doi.org/10.1016/j.ijthermalsci.2017.07.019.
[34] S. So, N. Jeong, A. Song, J. Hwang, D. Kim, C. Lee, Measurement of temperature and H_2O concentration in premixed CH_4/air flame using two partially overlapped H_2O absorption signals in the near infrared region, J. Applied sciences 11 (2021) 3701, https://doi.org/10.3390/app11083701.
[35] P. Dagaut, F. Lecomte, Experiments and kinetic modeling study of NO-reburning by gases from biomass pyrolysis in a JSR, J. Energ. Fuel. 17 (2003) 608–613, https://doi.org/10.1021/ef020256l.
[36] J. Kim, S. Jung, K.A. Lin, J. Rinklebe, E.E. Kwon, Comparative study on carbon dioxide-cofed catalytic pyrolysis of grass and woody biomass, J. Bioresource Technol. 323 (2021) 124631–124633, https://doi.org/10.1016/j.biortech.2020.124633.
[37] D.K. Seo, S.S. Park, J. Hwang, T. Yu, Study of the pyrolysis of biomass using thermo-gravimetric analysis (TGA) and concentration measurements of the evolved species, J. J. Anal. Appl. Pyrol. 89 (2010) 66–73, https://doi.org/10.1016/j.jaap.2010.05.008.
[38] C. Ji, D. Wang, J. Yang, S. Wang, A comprehensive study of light hydrocarbon mechanisms performance in predicting methane/hydrogen/air laminar burning velocities, J. Int. J. Hydrogen Energ. 42 (2017) 17260–17274, https://doi.org/10.1016/j.ijhydene.2017.05.203.
[39] J. Chen, G. Chen, A. Zhang, H. Deng, X. Wen, F. Wang, W. Sheng, H. Zheng, Numerical simulation of the effect of CH_4/CO concentration on combustion characteristics of low calorific value syngas, J. ACS omega 6 (2021) 5754–5763, https://doi.org/10.1021/acsomega.0c06176.
[40] M. Shim, K. Noh, W. Yoon, Flame structure of methane/oxygen shear coaxial jet with velocity ratio using high-speed imaging and OH, CH chemiluminescence, J. Acta Astronaut. 147 (2018) 127–132, https://doi.org/10.1016/j.actaastro.2018.03.053.
[41] H. Zhu, C. Hu, Q. Guo, Y. Gong, G. Yu, Investigation on chemiluminescence and structure characteristics in CH4/O2 diffusion flames, J. Exp. Therm. Fluid Sci. 102 (2019) 595–602, https://doi.org/10.1016/j.expthermflusci.2018.10.017.
[42] Y. Liu, J. Tan, M. Wan, L. Zhang, X. Yao, Quantitative measurement of OH* and CH* chemiluminescence in jet diffusion flames, J. ACS Omega 5 (2020) 15922–15930, https://doi.org/10.1021/acsomega.0c01093.
[43] G.P. Smith, J. Luque, C. Park, J.B. Jeffries, D.R. Crosley, Low pressure flame determinations of rate constants for OH(A) and CH(A) chemiluminescence, J. Combust. Flame. 131 (2002) 59–69, https://doi.org/10.1016/S0010-2180(02)00399-1.
[44] M.G. Davis, W.K. McGregor, A.A. Mason, OH chemiluminescent radiation from lean hydrogen-oxygen flames, J. The Journal of Chemical Physics 61 (1974) 1352–1356, https://doi.org/10.1063/1.1682059.
[45] M. Tamura, P.A. Berg, J.E. Harrington, J. Luque, J.B. Jeffries, G.P. Smith, D. R. Crosley, Collisional quenching of CH(A), OH(A), and NO(A) in low pressure hydrocarbon flames, J. Combust. Flame. 114 (1998) 502–514, https://doi.org/10.1016/S0010-2180(97)00324-6.
[46] K.T. Walsh, M.B. Long, M.A. Tanoff, M.D. Smooke, Experimental and computational study of CH, CH, and OH in an axisymmetric laminar diffusion flame, J. Symposium (international) on combustion 27 (1998) 615–623, https://doi.org/10.1016/S0082-0784(98)80453-0.
[47] G.P. Smith, C. Park, J. Schneiderman, J. Luque, C_2 Swan band laser-induced fluorescence and chemiluminescence in low-pressure hydrocarbon flames, J. Combust. Flame. 141 (2005) 66–77, https://doi.org/10.1016/j.combustflame.2004.12.010.
[48] M. Zhang, J. Wang, Y. Xie, Z. Wei, W. Jin, Z. Huang, H. Kobayashi, Measurement on instantaneous flame front structure of turbulent premixed CH_4/H_2/air flames, J. Exp. Therm. Fluid Sci. 52 (2014) 288–296, https://doi.org/10.1016/j.expthermflusci.2013.10.002.